Chapter 4
Remote Sensing in Mineral Exploration

4.1 Concept

Remote sensing was first adopted as a technique for obtaining information of distance objects without being in physical contact to the object (Fisher 1975). In practical terms remote sensing collects electromagnetic or acoustic signals. Earliest aerial were taken in 1858 from a balloon. However, since 1930 aerial photography using aircraft has been used extensively for resources survey. Satellite photography of the earth has been available to geologists since the early 1960s. Several hundred high oblique satellite photographs were acquired with a 70 mm hand-held camera during one of the Mercury missions in 1961. First formal geologic photography experiment (Gemini Mission) was carried out in 1965 (Lowman 1969). The multispectral terrain photography experiment on Apollo 9, which used four Hasselbled cameras and four different film–filter combinations, acquired 90 sets of photographs on 70 mm film between 3 and 13 March 1969. The success of the Apollo 9 experiment set the stage for both the Landsat programme and the Skylab Project. Operational usage of remote sensing were adopted and continue at present with the launch of remote sensing satellites like Landsat series (USA), SPOT series (France), Skylab(USA), IRS series (India), ERS series (Europe), MOS series (Japan), JERS-l (Japan) and ASTER (Japan and USA). Several high resolution satellites were also launched that could be used in geological high resolution mapping projects.

Remote sensing has gained importance due to its applications in various mineral exploration scenarios. The ore bodies may be associated with specific rock types, controlled by geological structures, and associated with different hydrothermal types. Some of geologically economic deposits such as laterite, bauxite show different morphological features. Remote sensing can help the exploration geologist to distinguished different rock types, map the hydrothermally altered rocks, investigate the morphological features and analyze the structural features.

G.S. Roonwal, *Mineral Exploration: Practical Application*,
Springer Geology, DOI 10.1007/978-981-10-5604-8_4

Today we utilize the remote sensing as a useful method in mineral exploration, since remote sensing helps in locating ore bodies that show up some surficial features such as geomorphology, hydrothermal alteration, structural features, lithology and geobotany.

4.2 Remote Sensing System

The link between the components of the remote sensing system is the electromagnetic (EM) energy. Electromagnetic energy disperse as wave energy with the velocity of light ($c = 3 \times 10^{10}$ cm/see). Here, we know that the source of EM radiation maybe originating from natural sources such as sun's reflected light or heat emitted by earth, or man-made, like microwaves. The physical or compositional properties of surface materials determine the amount and characteristics of the EM radiation. The sun is the principal source of EM radiation. The EM radiations incident on the earth's material can get absorbed or reflected. The reflectance can be specular, diffused and scattered. Remote sensing data can be classified based on the wavelength. The visible region spans between 0.4 and 0.7 μm. Near-infrared region is 0.7–1.0 μm (VNIR). Short-wave infrared (SWIR) begins from one micrometre and ends with three micrometres. The thermal infrared (TIR) considered to be 3–20 μm. The microwave region is between 1 cm and 1 m. Hence, we can classify remote sensing systems into optical and radar remote sensing.

The energy received by the sensor is then converted to analogue or digital form either onboard the spacecraft/airborne sensor or on the ground. The raw data received by the ground station usually needs to be preprocessed in order to make them usable for the end users (e.g. atmosphere and geometric corrections) (Lillesand and Keiffer 2000).

4.2.1 Remote Sensing Sensors

Remote sensing sensors acquire data in different wavelengths that is called spectral band. Each spectral band registers electromagnetic radiation in specific band region of electromagnetic spectrum. There are several remote sensing satellites that are imaging the Earth's surface. Although digital images of Landsat, ASTER, IRS and SPOT are well known amongst the geologists, but ASTER and Landsat images are more popular due to their spectral capabilities for geological mapping.

4.2.1.1 Landsat and ASTER Systems

Landsat data have mostly been used semi-arid or desert setting. It helps in locating for example iron oxides (gossan/oxidation) or even hydrous minerals such as

Table 4.1 Characteristics of ETM+ and Landsat-8 images

	Landsat 7	Landsat 8
Spectral bands	7	11
VNIR resolution (m)	30	30
SWIR resolution (m)	30	30
TIR resolution (m)	120	100
PAN resolution (m)	15	15
Spectral bands	μm	μm
Band-1	0.45–0.52	0.433–0.453
Band-2	0.52–0.60	0.450–0.515
Band-3	0.63–0.69	0.525–0.600
Band-4	0.76–0.90	0.630–0.680
Band-5	1.55–1.75	0.845–0.855
Band-6	10.4–12.5	1.56–1.66
Band-7	2.08–2.35	2.1–2.3
Band-8	0.5–0.9	0.5–0.68
Band-9	–	1.36–1.39
Band-10	–	10.30–11.30
Band-11	–	11.50–12.50

gypsum or even hydrothermal alteration. Table 4.1 shows the characteristics of different bands of ETM+ and Lansat 8 images.

The ASTER is an imaging instrument on the Terra platform. The satellite is a cooperative effort between NASA and Japan's Ministry of International Trade and Industry. ASTER obtains information on surface emissivity, temperature, reflectance and elevation. ASTER obtains data in 14 spectral channels from the visible through thermal infrared regions of the EM. It consists of three separate instrument subsystems (Abrams et al. 2002). Individual bandwidths and subsystems characteristics are summarized in Table 4.2. Theoretically, the SWIR bands of ASTER

Table 4.2 ASTER characteristics (Abrams et al. 2002)

Band	VNIR spectral resolution (mm)	Band	SWIR Spectral resolution (mm)	Band	TIR spectral resolution (mm)
1(nadir)	0.52–0.60	4	1.600–1.700	10	8.125–8.475
2(nadir)	0.63–0.69	5	2.145–2.185	11	8.475–8.825
3(nadir)	0.76–0.86	6	2.185–2.225	12	8.925–9.275
3(back ward)	0.76–0.86	7	2.235–2.285	13	10.25–10.95
		8	2.295–2.365	14	10.95–11.65
		9	2.360–2.430		
Technology detector	Pushbroom Si		Pushbroom PtSi:Si		Whiskbroom Hg: Cd:Te
Spatial resolution (m)	15 × 15		30 × 30		90 × 90
Swath width	60 km		60 km		60 km
Quantization	8 bits		8 bits		8 bit

have more capability than the Landsat for recognition of areas with hydrothermal alteration.

4.2.1.2 Indian Remote Sensing Satellites (IRS Series)

In India Remote Sensing is conducted by in Indian Space Research Organization's (ISRO)—Indian Remote Sensing satellites (IRS) series Earth observation satellites. Today there are also OceanSat, CartoSat, ResourceSat and others in the series. Table 4.3 shows specifications of these satellites.

Hyperspectral Imaging

The sensors that acquire several hundreds of spectral bands over a single area are called hperspectral imagers. These images are capable of mapping mineralogical composition present at the surface of the Earth. Thus, the airborne visible-infrared imaging spectrometer (AVIRIS) and HyMap are the airborne hyperspectral sensors which are capable of acquiring as many as 200 images over a single area.

The EO-1 (Earth observation) Hyperion is the only available space borne hyperspectral data available till today (Kruse et al. 2003). The imageries for this sensor is available free at www.USGS.gov. You may find lots of information related to characteristics of the sensors onboard EO-1 from this website.

Characteristics of Satellite Images

Each spectral band consists of columns and rows of pixels. Every pixel has an address in an image that can be shown as BVijk. BV stands for brightness value for each pixel, *i* and *j* represent column and row numbers, respectively, and k represents the spectral band number. For example in Fig. 4.2, the highlighted pixel in band-1 can be addressed as $52_{1822,\ 696,\ 1.}$

Figure 4.1 shows a subset of six spectral bands of ETM+ data over an area that contains vegetation cover (with black pixels in bands 1 and 3) and a hydrothermal alteration (with bright pixels in band 5). An enlarged portion of this image that is shown with a red square is shown in Fig. 4.2. The corresponding BVs or digital numbers (DNs) are also shown. Every surface feature may absorb electromagnetic energy in one wavelength and reflects in another. Therefore, in a grey scale image the features are in shades of grey. For example, the vegetation cover that is seen with dark pixels in bands 1, 2, 3 and 7; appears in higher DNs in band 4. This is due to the fact that green vegetation cover has absorptions in bands 1, 3 and 7 and reflection in band 4 of ETM+ images. The pixels covering the hydrothermally altered areas have higher BVs in band 5 and lower BVs in band 7. This phenomenon can be used in later sections for enhancing vegetation cover and hydrothermally altered rocks.

Table 4.3 Major specifications of IRS series of satellites (Navalgund et al. 2007)

Satellites (year)	Sensor	Spectral bands (μm)	Spatial res. (m)	Swath (km)	Radiometric res. (bits)	Repeat cycle (days)
IRS-IA/1B (1988, 1991)	LISS-I	0.45–0.52 (B) 0.52–0.59 (G) 0.62–0.68 (R) 0.77–0.86 (NIR)	72.5	148	7	22
	LISS-II	Same as LISS-I	36.25	74	7	22
IRS-P2 (1994)	LISS-II	Same as LISS-I	36.25	74	7	24
IRS-1C/1D	LISS-II	0.52–0.59 (G), 0.62–0.68 (R) 0.77–0.86 (NIR) 1.55–1.70 (SWIR)	23.5 70.5 (SWIR)	141 148	7	24
	WiFS	0.62–0.69 (R) 0.77–0.86 (NIR)	188	810	7	24(5)
	PAN	0.50–0.75	5.8	70	6	24(5)
IRS-P3 (1996)	MOS-A MOS-B MOS-C WiFS	0.755–0.768 (4 bands) 0.408–1.010(13 bands) 1.6 (1 band) 0.62–0.68 (R) 0.77–0.86 (NIR) 1.55–1.70 (SWIR)	1570 × 1400 520 × 520 520 × 640 188	195 200 192 810	16 16 16 7	24 24 24 5
IRS-P4 (1999)	OCM MSMR	0.402–0.885 (8 bands) 6.6, 10.65, 18, 21 GHz (V & H)	360 × 236 150, 75, 50 and 50 km, respectively	1420 1360	12 –	2 2
IRS-P6 (2003)	LISS-IV	0.52–0.59 (G) 0.62–0.68 (R) 0.77–0.86 (NIR)				

(continued)

Table 4.3 (continued)

Satellites (year)	Sensor	Spectral bands (μm)	Spatial res. (m)	Swath (km)	Radiometric res. (bits)	Repeat cycle (days)
	LISS-III	0.52–0.59 (G), 0.62–0.68 (R) 0.77–0.86 (NIR) 1.55–1.70 (SWIR)	5.8 23.5	70 141	10(7) 7	24(5) 24
	AWiFS	0.52–0.59 (G) 0.62–0.68) (R) 0.77–0.86 (NIR) 1.55–1.70 (SWIR)	56	737	10	24(5)
IRS-P5 (Cartosat-I) 2005	Pan (Fore (+26°) & Aft (−5°))	0.50–0.85	2.5	30	10	5
Cartosat-2 (2007)	PAN	0.50–0.85	0.8	9.6	10	5

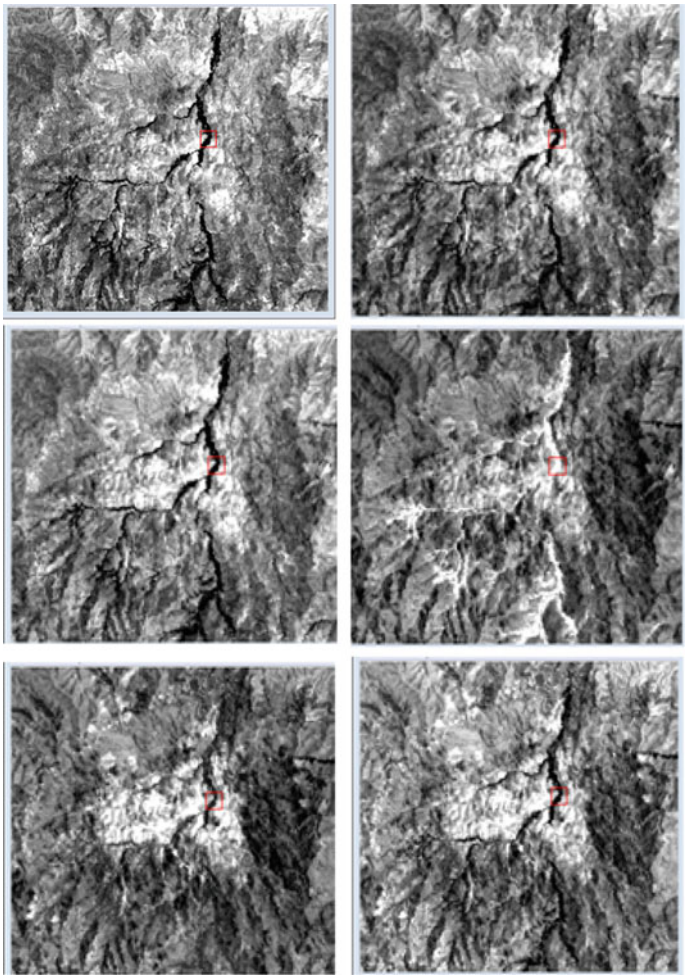

Fig. 4.1 Six images of ETM+ that show an area with hydrothermal alteration and vegetation cover

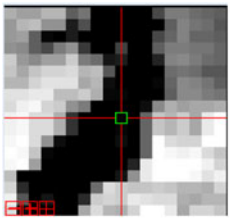

	1818	1819	1820	1821	1822	1823	1824	1825	182
690	71	59	49	48	60	46	44	64	68
691	79	68	66	54	55	44	42	56	69
692	81	76	77	63	46	42	43	51	66
693	82	74	76	53	48	45	44	52	65
694	77	79	75	52	52	47	47	48	64
695	71	68	50	46	46	43	53	70	75
696	58	50	44	45	52	43	65	78	76
697	58	50	44	45	52	43	65	78	76
698	46	46	44	46	53	45	65	88	81
699	46	43	42	44	45	50	65	91	85
700	43	45	43	45	45	56	83	93	86
701	49	44	44	44	54	71	83	94	87
702	42	47	66	81	79	78	78	79	78
703	43	57	79	80	79	83	82	81	81

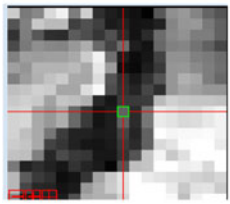

	1818	1819	1820	1821	1822	1823	1824	1825	182
690	94	100	80	69	81	58	55	80	87
691	99	109	120	82	58	53	56	69	92
692	104	99	117	95	54	52	58	66	93
693	99	98	114	74	63	57	64	74	93
694	98	114	122	72	64	60	70	63	93
695	105	101	61	56	66	66	67	104	110
696	80	66	55	58	78	62	84	118	116
697	80	66	55	58	78	62	84	118	116
698	59	59	57	58	69	60	78	124	121
699	59	56	55	57	66	62	78	113	116
700	66	65	56	56	64	74	107	121	108
701	64	60	57	51	74	105	107	124	124
702	55	65	97	108	116	127	118	116	114
703	57	94	101	109	115	128	131	128	118

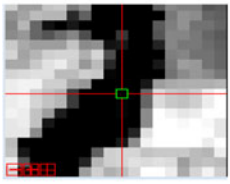

	1818	1819	1820	1821	1822	1823	1824	1825	182
690	71	62	49	48	58	42	42	63	71
691	81	72	73	52	53	40	39	55	71
692	84	78	84	62	40	36	41	49	70
693	83	74	80	56	44	40	41	53	69
694	80	83	82	50	48	40	47	47	68
695	76	74	45	42	45	45	53	75	77
696	59	49	39	42	50	42	66	85	82
697	59	49	39	42	50	42	66	85	82
698	43	42	37	42	50	43	72	95	89
699	43	39	39	40	44	46	72	97	91
700	43	39	37	41	45	55	86	101	91
701	45	41	40	40	53	72	89	102	95
702	39	42	65	83	84	84	81	82	82
703	39	55	79	83	84	86	85	86	85

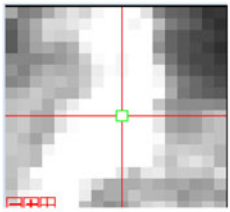

	1818	1819	1820	1821	1822	1823	1824	1825	182
690	90	103	116	134	111	112	109	83	74
691	88	96	105	113	104	116	122	91	77
692	90	94	102	105	104	116	118	103	81
693	91	95	103	108	108	111	120	104	87
694	90	97	107	116	106	120	139	111	89
695	102	106	117	118	147	151	126	94	84
696	105	113	123	117	137	146	120	101	87
697	105	113	123	117	137	146	120	101	87
698	109	116	125	116	120	124	113	105	92
699	109	115	118	125	138	122	113	102	95
700	130	126	117	120	121	109	109	99	93
701	122	131	113	106	101	93	101	102	94
702	109	103	97	89	89	89	91	89	87
703	111	102	86	89	89	94	91	91	90

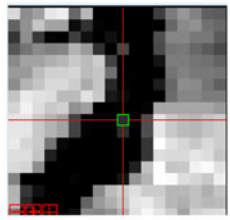

	1818	1819	1820	1821	1822	1823	1824	1825	182
690	82	76	51	38	56	33	28	57	67
691	87	84	88	55	37	30	28	44	69
692	90	84	86	66	33	29	33	38	67
693	88	80	86	49	40	32	34	46	64
694	84	93	87	45	42	32	36	34	65
695	74	77	35	30	32	32	40	79	79
696	55	40	30	34	50	30	58	94	87
697	55	40	30	34	50	30	58	94	87
698	33	33	29	32	39	32	52	102	93
699	33	28	27	30	34	34	52	92	91
700	34	33	27	28	35	47	85	101	86
701	40	32	31	30	44	75	82	100	99
702	28	38	72	84	88	92	88	88	83
703	33	63	76	81	86	94	95	90	83

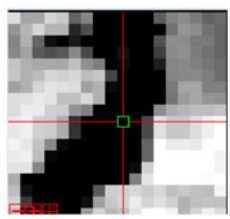

	1818	1819	1820	1821	1822	1823	1824	1825	182
690	87	71	46	42	57	37	36	68	87
691	101	89	84	51	55	35	30	60	86
692	107	100	103	70	37	30	35	49	86
693	108	93	97	55	40	33	34	51	83
694	101	107	97	49	47	34	36	45	82
695	90	85	42	33	32	31	53	88	96
696	65	51	29	36	46	32	71	109	103
697	65	51	29	36	46	32	71	109	103
698	39	37	29	36	48	36	78	123	112
699	39	32	29	35	36	43	78	125	117
700	35	27	28	34	36	55	105	125	117
701	38	33	31	32	54	85	110	130	121
702	35	38	75	104	105	107	104	107	101
703	32	56	93	103	106	112	106	109	105

Fig. 4.2 An enlarged portion of Fig. 4.1 with *grey* scale images and corresponding DNs

4.2.2 EM Spectrum

Electromagnetic spectrum is a continuum consisting of the ordered arrangement of radiation according to the wavelength, frequency or energy. It extends from highly energetic cosmic rays photons through gamma rays, X-rays, ultraviolet, visible, infrared, microwave and radiowaves. The wavelengths that are greatest interest in remote sensing are visible and near-infrared radiation.

4.2.3 Spectral Characteristics of Hydrothermal Alteration Minerals

A group of minerals could be used as index minerals that occur in the altered rocks associated with various mineral deposits such as porphyry copper deposits. The spectral properties of minerals can be used for their identification, based on their reflectance behaviour. The spectral reflectance characteristics of rocks and minerals in the visible near-infrared (VNIR) through the short-wave infrared (SWIR) wavelength regions (0.4–2.5 μm) are the result of different physical and chemical properties. However, the spectral feature that is typically displayed by the well-defined bands is caused by absorptions due to both electronic and vibration processes in the individual mineral constituents (Hunt and Salisbury 1970; Hunt and Ashley 1979). Here, we are concerned with the process that leaves to locating the mineral deposits. Between 0.35 and 1.3 μm, electronic transitions in the iron-bearing minerals (hematite, goethite and jarosite) cause characteristic features, in the form of minima, to occur near 0.43, 0.65, 0.85 and 0.93 μm. They are common components in many ore minerals and indicating iron oxide-rich caps,

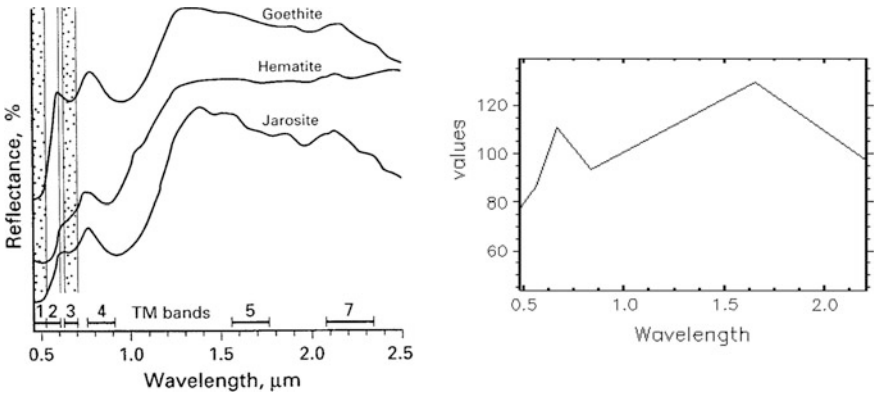

Fig. 4.3 **a** Spectral pattern of oxidized zone—gossan for jarosite, hematite and goethite and **b** Spectral profile on an area rich in iron oxide. Note the peak in band 3 and an absorption feature in band-1 of ETM+ data

known as gossan. Figure 4.3 depicts the spectra of three iron oxide bearing samples that show absorption in blue band (band 1) due to electronic process (charge-transfer) and reflections in red and near-infrared (NIR) portions (bands 3 and 4). This explains why we see oxidize zone in form of gossan which contain hematite in red and brown.

The oxidation process and products generated comprise within it hydrous (OH) molecules or even carbonate associated minerals of Al, Fe, Mg as aluminium ore, iron ore or MgOH. They constitute clays, sulphates and water-bearing minerals (alunite, kaolinite, illite, montmorillonite, Pyrophyllite, mica, diaspore, jarosite, chlorite and carbonates) that are common in the hydrothermally altered rocks (Hunt and Ashley 1979). Figure 4.4 depicts the spectrum. These mineral have an absorption feature within band 7 and a reflection in band 5 of ETM+, respectively. Here, the bands ETM+ and ASTER sensors can distinguished between clay minerals and alunite, while, ETM+ images is not able to do so, due to the fact that band 7 has more width and covers all absorption features.

Since ASTER and Landsat data are widely used by the geologist around the world more than any other satellite systems, here the spectral properties of rocks and minerals are explained based on the spectral bands of these data. The ASTER, VNIR + SWIR pattern of mineral generated due to hydrous nature of mineral can be seen clearly. These mineral comprise micas (sericite) illite in rock such as phyllite. The rock basically consists of clays—kaolinite (Fig. 4.5).

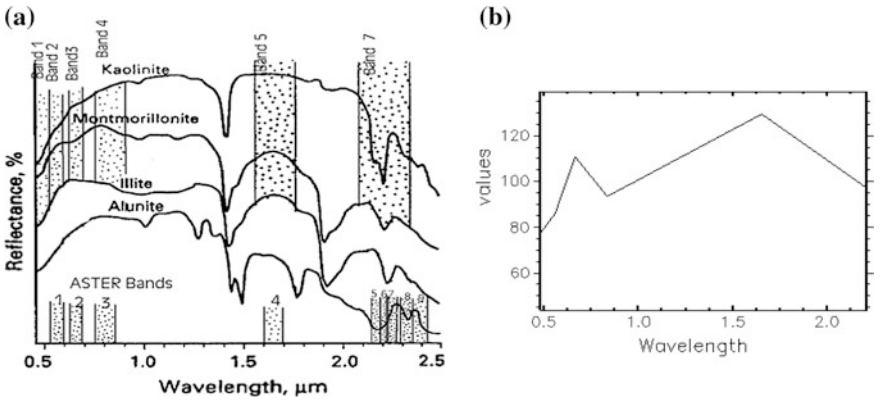

Fig. 4.4 **a** Showing reflectance spectra of clay minerals. The bands widths of TM and ASTER are shown. **b** The relative reflection over an altered area

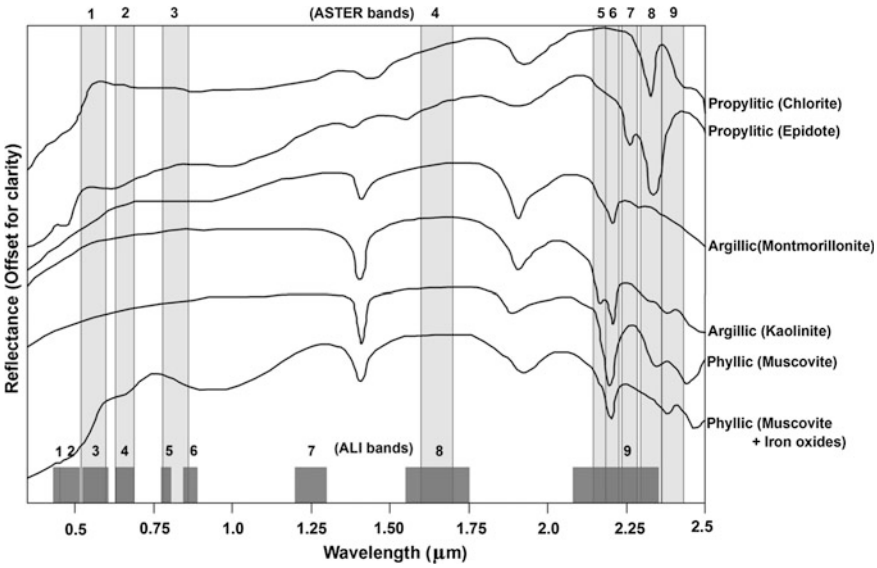

Fig. 4.5 Showing a Laboratory Reflectance Spectra of important hydrothermal alteration minerals. ASTER and ALI bands are shown in figure (Honarmand et al. 2011)

4.3 Discrete or Digital Image Processing of Satellite/Airborne Images

Gillespie (1980), Hord (1982, 1986), Swain and Davis (1978), Lillesand and Kiefer (1987, 1994), Niblack (1986), Mather (2001), Jensen (1996) and Gupta (2003) have given reviews in digital image processing of remote sensing data. A digital image comprises a number of individual picture elements called Pixels, each one having an intensity value (Digital number) and an address in two dimensional image space, i.e. rows and columns The digital number (DN) may represent the reflectance of EM radiation (albedo, emissivity, temperature) or some geophysical, geochemical or topographical data. The DN value is dependent of the intensity range of the image which usually stretches from minimum (0) to maximum (255 in 8 bit format). The image data are usually stored in computer compatible tapes (CCT), floppy disks, data cartridges, digital audio tapes (DAT) and CD-ROM medium.

We understand that the digital image processing is carried out by computer processing of digital data generated. In general the purpose of digital image processing is to enhance or improve the image quality to extract information from it. Digital image processing offers precision and flexibility over optical or electrical methods. Voluminous data becomes a challenging task to analyze within a limited time. Use and application has helped greatly in data processing and time saving. Many useful digital image processing operations are available on personal computers and desktop workstations (Niblack 1986).

Digital image processing generally involves image correction, image registration, image enhancement, image segmentation and image classification depending on the objectives of the study. In the present study, image registration and image enhancements have been used. Image enhancement broadly comprises of (i) single image enhancement and (ii) multiple image enhancement.

4.3.1 Image Registration

Image registration involves the geometric transformation in an image. The aim of geometric restoration and correction is to generate an image which can be registered or align, with some standards, e.g. maps of the area covered by an image or another rectified image of the same area. Ground control points (GCPs) are needed for registration process. Few GCPs we chosen which can be recognized easily both in the image as well as the map (e.g. stream junctions, road intersection, etc.). The GCPs are fed into the computer and based on the GCP coordinates, the image is subjected to coordinate transformation according to a set of equations called affine projections. The coordinate of the two sets of GCPs defines the transformation parameters. Typically a set of two equations (affine projections) is used to link the two coordinate systems:

$$X' = a0 + a1x + a2y + a3xy$$
$$Y' = b0 + b1x + b2y + b3xy$$

where X' and Y' are the coordinates in the new system, and x and y are the coordinates of the same points in the map. $a1$, $a2$, $a3$, $b0$, $b1$, $b2$ and $b3$ are the unknown constants which can be computed using four control points. To use the above equations to geometrically transform an image four stages are required. First, a geometrically correct geographical grid is defined in terms of latitude, longitude or northing and easting. Second, the computer proceeds through each cell in this geographical grid and at each cell the computer transforms the latitude/longitude or northing/easting values into values of x and y which becomes the new address of an image pixel. Third, the computer visits this address in the image and transfers the appropriate DN by interpolation. Forth, this process is repeated until the geographical grid is full at which point the image has been geometrically correlated (Bernstein 1983).

4.3.2 Image Enhancement

Image enhancement involves the processes applied on the images in order to improve the image quality so as to make them more interpretable. By applying a

particular enhancement technique some features may become better discernible at the cost of other features, e.g. directional filtering enhances the linear features at a particular directions though other features in the image is suppressed. A particular band ratio may enhance vegetation cover and another ratio may enhance the iron oxide or argillic alteration. There are several methods of image enhancement, such as (1) contrast stretching, (2) band rationing, (3) principal component analysis, (4) addition and subtraction, (5) RGB coding, (6) spectral angle mapper and (7) image filtering.

4.3.3 Contrast Stretching

Here, monitor screen of processor, or the light source in a digital film writer is from 0(zero-black) to 255(maximum intensity), but in general, pixels in an image often occupy a small portion of the possible range of grey-level values, resulting in low-contrast display on which some features might be indistinguishable. Image processing software can change any DN in an image to any of 255 intensity levels. The stretching is done by spreading the DNs equally over the 0–255 range. The minimum DN is set to 0 and the maximum to 255 with other DNs falling between these two extreme values. Guides to distinguished or identified even minor variation is observed. Different methods of contrast stretching such as linear contrast stretching, multiple linear stretching, logarithmic, power or functional stretching, Gaussian stretching, histogram equalization stretching and density slicing are available in the modern image processing softwares. In all cases the images are stretched.

4.3.4 Band Rationing

Band rationing or spectral rationing is an extremely useful procedure for enhancing features in the multispectral images. In this technique, the DN values of one band is divided by the corresponding DN values of another band, pixel by pixel, and the resultant data is rescaled to fill the dynamic range of the display device by contrast stretching operation. Ratio images are useful because they have the effect of suppressing the detail in a scene which is caused by topographic effects (i.e. variable effects of illumination conditions) while enhancing colour boundaries. This property has made ratio pictures quite useful in geological applications because they exaggerate subtle colour differences in a scene and many geological problems require distinction between rock types that may appear quite similar. Ratio images are interpreted because they can be directly related to the spectral properties of materials. More information can be obtained by using those ratios that maximize the differences in the spectral slopes of materials in the scene. Rationing technique has been used to enhance argillic verses non-argillic, rock versus vegetation, iron oxide

Table 4.4 ASTER band ratio for enhancing mineral features (based on van der Meer et al 2012)

Mineral feature	ASTER bank combinations(2)
Ferric iron	2/1
Ferrous iron	5/3 and 1/2
Ferric oxide	4/3
Gossan	4/2
Carbonate/Chlorite/Epidote	(7 + 9)/8
Epidote/Chlorite/Amphibole	(6 + 9)/(7 + 8)
Amphibole	(6 + 9)/8 and 6/8
Dolomite	(6 + 8)/7
Carbonate	13/14
Sericite/Muscovite/Illite/Smectite	(5 + 7)/6
Alunite/Kaolinite/Pyrophyllite	(4 + 6)/5
Phengite	5/6
Kaolinite	7/5
Silica	11/10, 11/12, 13/10
SiO_2	13/12, 12/13
Siliceous rocks	(11 × 11)/(10 × 12)

versus non iron oxide (Drury and Hunt 1989). A disadvantage of rationing is that it suppresses differences in albedo. The rocks such as basalt and marls will appear the same in the ratio image, though they have a lower and a higher albedo, respectively. Table 4.4 presents few band ratios for enhancing mineral features.

It is possible to use, apart from the simple rationing, the output images resulted from the other image enhancement techniques (e.g. PC images, ISH images, added and subtracted images, etc.) as either denominator or numerator. This technique may provide in some cases, useful information for geological studies.

4.3.5 Addition and Subtraction

Subtraction and addition of satellite images are simple and useful methods of image enhancement when the multispectral images are highly correlated. Addition of spectral images generates an image with much larger dynamic range than original images. Therefore, higher contrast image is the result. The image which is produced by differences of two images is characterized by lower contrast. This technique particularly enhances the areas which are less correlated in the original images and therefore it is possible to derive change-detection image from multispectral data. Image subtraction sometimes can give the same result as image ratio but with much simpler operation (Navai and Mehdizadeh-Tehrani 1994).

4.3.6 Principal Component Analysis (PCA)

The principal component analysis is a multivariate technique that selects uncorrelated linear combinations (eigenvector loadings) of variables in such a way that each successively extracted linear combination, or PC, has a smaller variance. Remove redundancy from the multispectral data is the main aim of PC analysis. Principal component analysis is extensively used for mapping of hydrothermal alteration in metallogenic provinces (Abrams et al. 1983; Loughlin 1991; Tangestani and Moore 2001, 2002).

A feature oriented principal component selection is known as Crosta technique. It allows identification of the principal components (through the analysis of the eigenvector values) that contain spectral information about specific minerals, as well as the contribution of each of the original bands to the components in relation to the spectral response of the materials of interest. This technique can be applied on four and six selected bands of Thematic Mapper (TM) data. The technique indicates whether the materials are represented as bright or dark pixels in the principal components according to the magnitude and sign of the eigenvector loadings.

4.3.7 Red-Green-Blue (RGB) Coding

The colour images are the result of the three additive primary colours (red, green and blue) in the RGB colour coordinate system. However, it is often difficult to choose proper band combination and produce an optimum FCC especially in the cases where several images are involved. Optimum index factor (OIF) may solve this problem up to some extent (Chaves et al. 1982). The technique uses the computation of total variance and correlation within and between bands. The combination with higher OIF is chosen for making false colour composite. Similar statistical method suggested by Hunt et al. (1986) and according to this method the most informative three spectral bands are the least well correlated ones.

4.3.8 Spectral Angle Mapper (SAM)

The Spectral Angle Mapper (SAM) allows mapping of the spectral similarity of image spectra to reference spectra. The reference spectra can be selected from either laboratory or field spectra or extracted from the image. Spectral analysis assumes a spectral angle which represents the data has been reduced to apparent reflectance, with all dark current and path radiance biases removed. SAM compares the angle between the reference spectrum and each pixel vector in n-dimensional space, and

smaller angles represent closer matches to the reference (Kruse et al. 1993). The angle can be calculated using following equation:

$$\propto = \cos^{-1}\left(\frac{\sum_{i=1}^{nb} i_i r_i}{\left(\sum_{i=1}^{nb} i_i^2\right)^{1/2}\left(\sum_{i=1}^{nb} r_i^2 r_i^2\right)^{1/2}}\right) \tag{4.1}$$

i_i and i_r are the image and reference spectra, respectively, and nb is the number of bands. Lower angle indicates more correlation between the image spectra and reference spectra.

The SAM algorithm has been used on hyperspectral and multispectral data for hydrothermal alteration mapping (Ranjbar and Honarmand 2007; Di Tommaso and Rubinstein 2007; Tangestani et al. 2008; Shahriari et al. 2013).

4.3.9 Image Filtering

Spatial filters emphasize or deemphasize image data of various spatial frequencies. Spatial frequency refers to the degree of changes in pixel values from one pixel to another. In a high frequency image, the tonal changes are abrupt (e.g. changes across lithological boarder). In contrast, a low frequency image has gradual tonal changes (e.g. tonal changes within a lithology or water body). Low pass filters are designed to emphasize low frequency features and deemphasize the high frequency components of an image (local detail). High pass filters emphasize the detailed high frequency components of an image and deemphasize the more general low frequency information. There are several low frequency filters such as mean, median, mode, Gaussian, etc. High pass filters include Laplacian, Sobel and Roberts. The high pass filters are of two types as follows:

1. The filters that enhance the high frequency features in all directions.
2. The filters that enhance the high frequency features in a specific direction.

For example, if enhancement of faults in a particular direction is desired, a directional filter can be applied. In cases where the lithological boundaries that may not have specific directions, Laplacian filter may be applied. Enhancement of drainage pattern in an image also can be done using Laplacian filter.

In order to digitally filter an image, a kernel is used. Figure 4.6 shows a Laplacian (A) and a high pass directional filters' kernels (B). The latter kernel can enhance the features in east–west direction. This kernel is moving over an image and a new value is calculated for the central pixel every time the kernel stops over nine pixels.

As mentioned earlier in the preceding chapters, many of ore deposits (such as porphyry and vein types) are associated with faults or lineaments. To enhance these features, the satellite images can be filtered with high pass filters. After this step, the

(a)

-1	*-1*	*-1*
-1	8	*-1*
-1	*-1*	*-1*

(b)

0	-2	0
0	4	0
0	-2	0

Fig. 4.6 Kernels for **a** Laplacian filter and **b** directional filter

lines showing the geological features should be drawn manually with a help of Geographic Information System (GIS) software.

Another aspect is the Photolineament Factor (PF) is applied for analyzing lineaments distribution and has application in mineral exploration, as suggested by Hardcastle (1995). Generally, in the system a grid with cell size (e.g. 2 × 2 km) is superimposed over the lineament map and each parameter is calculated from the respective cells. The photolineament factor value is calculated using the following equation:

$$\mathrm{PF} = a + b + c \tag{4.2}$$

where '*a*' is number of lineament intersections in each cell/average of the area, '*b*' is number of lineaments in each cell/average of the area and '*c*' is number of major lineament directions in each cell/average of the area. According to our study (Ranjbar and Roonwal 2002) the PF values are thus controlled. Our study further showed that in known occurrence of mineralization zones even in highly altered condition, this method is very useful.

4.4 Application of Remote Sensing in Mineral Exploration

As mentioned earlier, mineralization may be associated with a particular lithology, geological structure, morphology, hydrothermal alteration, etc. remote sensing may help mapping or enhancing these geological features especially in the arid/semi-arid parts of the world. Here, few geological features are investigated using remote sensing.

4.4.1 Geological Structures

It is an established fact that some of ore bodies, petroleum/gas reservoirs are controlled by geological structures. Here, several types of structures are shown that depict the ability of remote sensing for mapping them. Figure 4.7 shows a plunging syncline in the eastern part of Iran that hosts coal beds. The rocks in the syncline are composed of sandstone, shale, limestone and marl of Jurassic age. The coal beds are seen in the shale and sandstone sequence. The southern limb of the fold is normal but the northern limb is inverted as shown in Fig. 4.7. The fold is plunging to the southeast direction.

The host lithology is a sequence of shale and sandstone that is seen in bluish colour in Fig. 4.8 that goes round the fold. This image helps the geologists to locate the coal beds in the coal–sandstone sequence in other parts of the fold. We know that folded structures are proper places for exploration of hydrocarbon. Some of these structures are outcropping at the surface that can be mapped by remote sensing. If these structures are covered by alluvium or other lithologies, they can be mapped by geophysical methods such as gravity and seismic. Here remote sensing can help the geophysists to lay down proper geophysical lines for data collection (Ranjbar 2011).

Figure 4.8 shows many double plunging anticlines in south of Iran. The outcropping lithology is limestone that belongs to the Asmari and Jahrom Formations which act as reservoirs while being enclosed with impermeable strata.

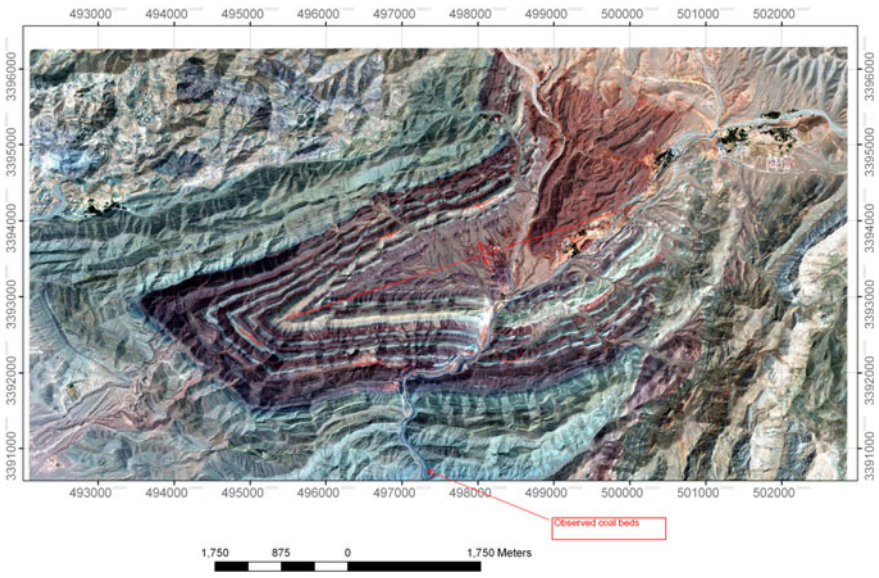

Fig. 4.7 Satellite image in true colour that shows a plunging syncline in east of Iran. The map coordinate is N, UTM, Zone 40, WGS84

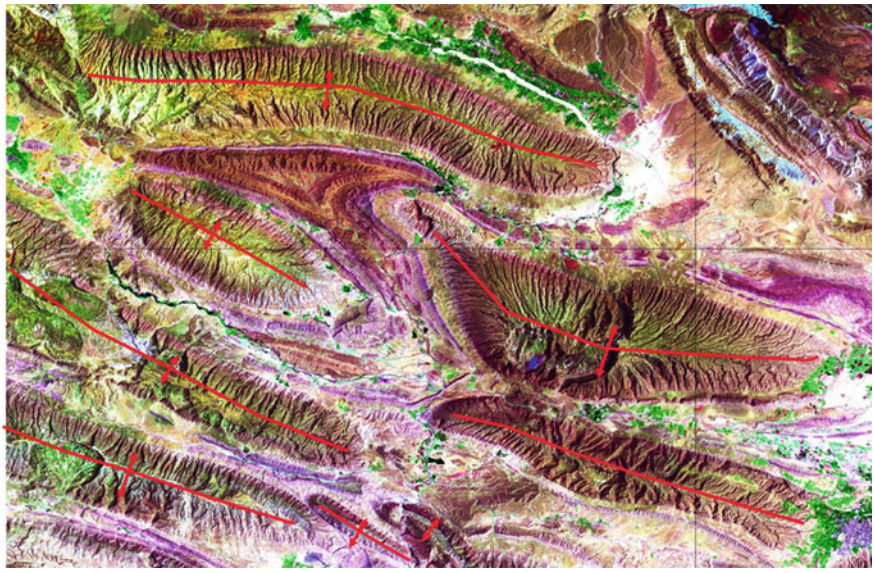

Fig. 4.8 Landsat image in false colour that shows doubly plunging anticlines in south of Iran (color figure online)

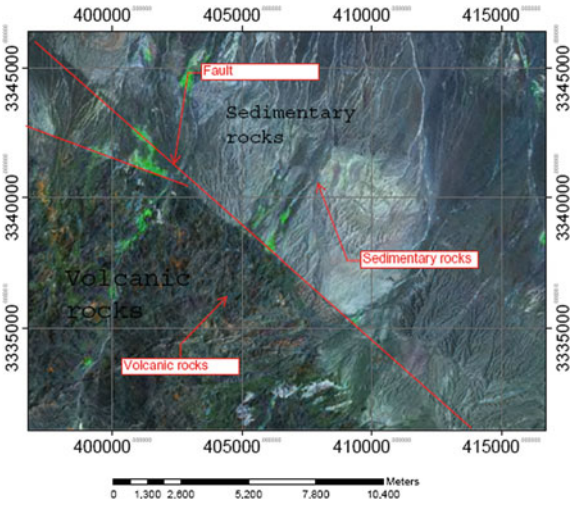

Fig. 4.9 Faults that separated volcanic from the sedimentary rocks. The map coordinate is N, UTM, Zone 40, WGS84

Here they are outcropping at the surface and do not contain hydrocarbon. Hydrocarbon may be present within the underlying strata. Faults are important structure in mineral exploration scenarios. They provide pathways for hydrothermal solutions, increase permeability, and act as barrier and traps for hydrocarbons.

Although the lithological changes are abrupt on both sides of a fault, it is very easy to detect it (Fig. 4.9). In cases where the fault has occurred in one lithology,

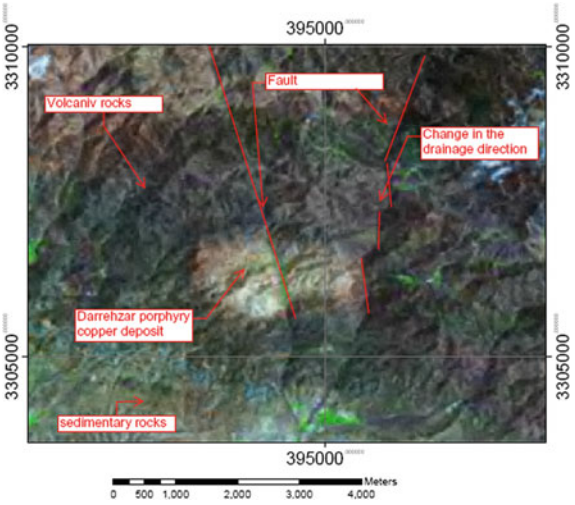

Fig. 4.10 A false colour image of landsat. Faults that cut across the Darrehzar intrusive body which hosts a porphyry copper deposit. The map coordinate is N, UTM, Zone 40, WGS84 (color figure online)

the changes in drainage pattern are used for its recognition. The faults are cutting across the Darrehzar intrusive which is a granodiorite that hosts a porphyry copper deposit in southeast of Iran (Fig. 4.10). On the eastern part, the drainage is dissected several times due to faulting.

Porphyry copper deposits are associated with faulting systems. The faulting increases permeability in the rock units that do not have primary permeability, provide the pathways for the hydrothermal solutions. In order to graphically show the areas with higher lineament density, photolineaments maps are prepared. Figure 4.11 depicts the Landsat image of an area located in the southeast Iran that hosts Sar Cheshmeh porphyry copper deposit and few smaller porphyry and vein type mineralization. This image is filtered, the lineaments were extracted and finally the PF value contours were drawn using Eq. 4.2. The copper deposits are associated with higher PF values.

4.4.2 Hydrothermal Alteration Mapping

As mentioned earlier in this chapter, exploratory remote sensing is mostly used for enhancing the hydrothermal alteration that may be associated with mineralization. Several image processing techniques such as band rationing, principal component analysis and spectral angle mapper can be used for mapping hydrothermal alteration types.

Porphyry copper deposits received large attentions for exploration by the remote sensing techniques all over the world. The associated zones of hypogene hydrothermal alteration and weathering are spatially large enough to be detected and mapped by using multispectral remote sensing data. Most of the known

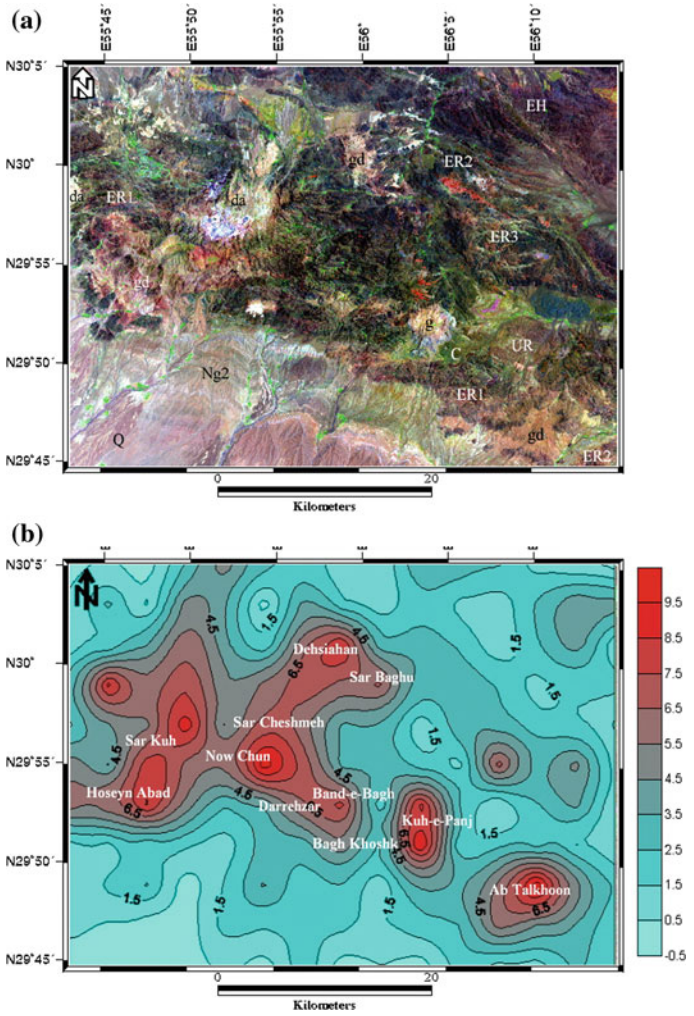

Fig. 4.11 **a** False colour image that shows lithological variation in the Sarcheshmeh area. EH, ER1, ER2, *ER3* volcanic rocks of Eocene, *gd* granodiorite, *dc* dacite, *Ng2* Neogene sedimentary rocks, *Q* Quaternary sedimens. **b** Photolineament factor value of the above image (color figure online)

Porphyry copper deposits are characterized by a well-developed zonal pattern of mineralization and wall rock alteration that can be defined by assemblages of hydrothermal alteration minerals. The most intense alteration occurs in the core of the porphyry body and diminishes radially outward in a series of concentric zones of alteration minerals (Fig. 4.12).

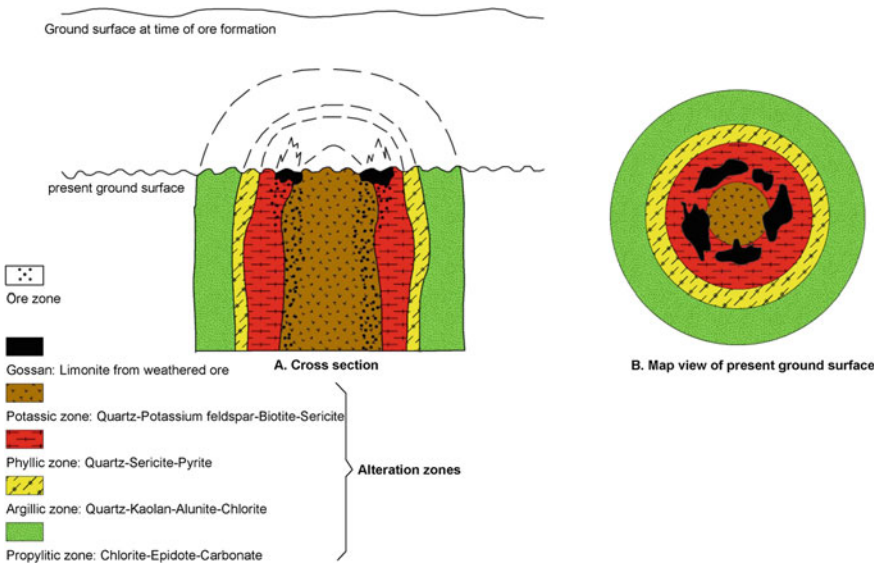

Fig. 4.12 Concept of hydrothermal alteration of porphyry copper deposit showing various rock-type zones such as, potasic, phyllic, argillic and propylitic alteration (modified from Sabins 1999)

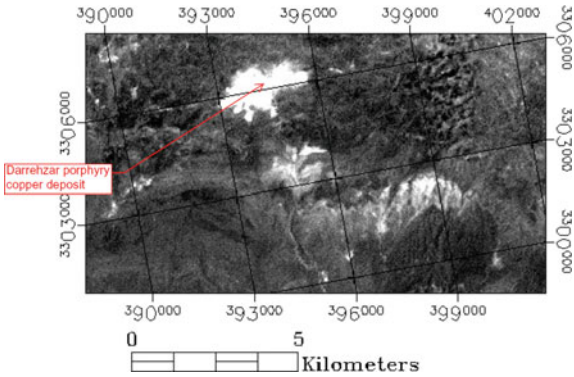

Fig. 4.13 Band 4/Band 6 ratio of ASTER data that shows hydrothermally altered areas with bright pixels

4.4.2.1 Band Ratio

It has been observed that hydroxide molecules of minerals form large halos because of hydrous nature. Examples of this are clearly seen in the minerals comprising sheet silicates since they contain Hydroxyl-bearing minerals form the most widespread products of hydrothermal alteration. An abundance of clays and sheet silicates, which contain Al–OH– and Mg–OH-bearing minerals and hydroxides in alteration zones, is characterized by absorption bands in the 2.1–2.4 μm due to

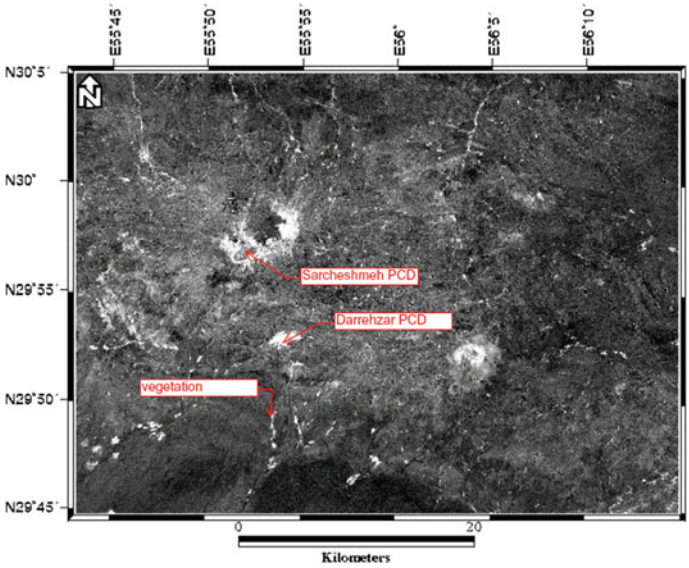

Fig. 4.14 Band 5/Band 6 of ETM+ data that depicts hydrothermal alteration with bright pixels

molecular vibrational processes (Fig. 4.4). Here, due to clays and sheet silicates higher reflectance in band 4 of ASTER data is observed. Here, common features of phyllosilicates have been recorded and utilized for mineral exploration (e.g. Galvao et al. 2005; Hubbard and Crowley 2005; Mars and Rowan 2006; Rowan et al. 2006).

Band ratio techniques though simple are important criteria in distinguishing and identifying remote sensing image analysis. It guides to spectral differences between bands as well as to help reduce influence of topography (Rowan and Mars 2003; Zhang et al. 2007). Distinguishing spectral bands produce an image that provides relative band intensities. The resulted image enhances the spectral differences between the bands. Areas with hydrothermal alteration are usually enhanced as bright pixels in images of band 4/band 9, band 4/band 5 and band 4/band 6 for clay and sheet silicates and 9/8 ratio for chlorite and epidote in ASTER data. Figure 4.13 shows band4/band6 for Darrehzar porphyry copper deposit. Figure 4.14 shows band 5/band 7 ratio images of Landsat ETM+ data. In both images the hydrothermally altered areas are enhanced with bright pixels. The area of this image covers the area shown in Fig. 4.11.

4.4.2.2 Principal Component Analysis

In Sect. 4.3.6 we have already discussed about principal component analysis, additional aspects of PCA are narrated here.

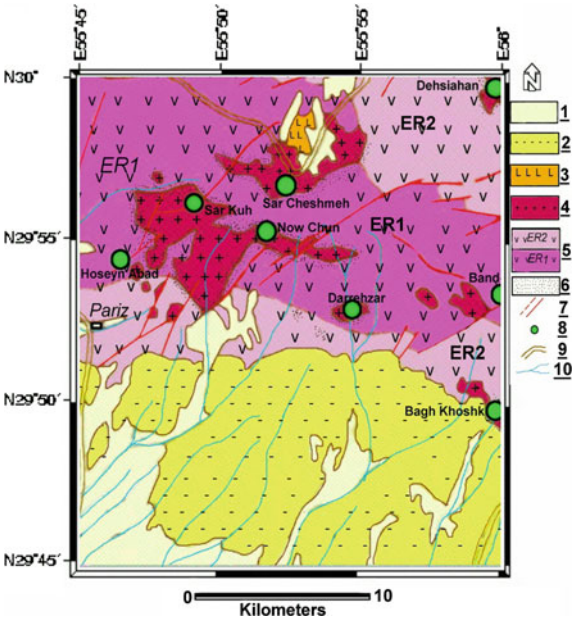

Fig. 4.15 Geology of porphyry copper deposit of Sar Cheshmeh, Kerman, Iran. Index shows: *1* Quaternary alluvium, *2* Quaternary gravel fan, *3* Quaternary calcareous terraces, *4* Neogene sediments, mostly arenites with pebbles and boulders of volcanic and intrusive rocks. Dacites and dacitic pyroclastics, *5* Granodiorite, quartz diorite, diorite porphyries and monzonite, dikes of Oligocene-Miocene age, *6* Eocene volcanic-sedimentary complex, trachyandesites, trachybasalts, basaltic andesites, pyroclastics, etc. *7* Fault, *8* Working mine and copper deposit, *9* hydrothermal alteration (after, Dimitrijevic et al. 1971)

Table 4.5 Eigenvector loadings for six bands of ETM+ data

	PC1	PC2	PC3	PC4	PC5	PC6
Band 1	0.26	−0.49	0.20	0.02	0.62	−0.50
Band 2	0.34	−0.39	0.18	−0.21	0.14	0.79
Band 3	0.49	−0.39	0.02	0.09	−0.72	−0.26
Band 4	0.34	0.010	−0.91	0.11	0.20	−0.37
Band 5	0.53	0.54	0.13	−0.62	0.05	0.05
Band 6	0.42	0.40	0.29	0.74	0.13	−0.16
% of variance	88	8.5	1.9	0.08	0.05	0.01

Standard PCA is applied on ETM+ data of Sar Cheshmeh area. The intrusive bodies are composed of diorite, quartz diorite and granodiorite of Oligocene–Miocene age that intrude Eocene Volcanic-Sedimentary complex comprised mainly of volcano-clastics, andesite, trachy-andesite and sedimentary rocks. The hydrothermally altered rocks are highly fractured, and supergene alteration has

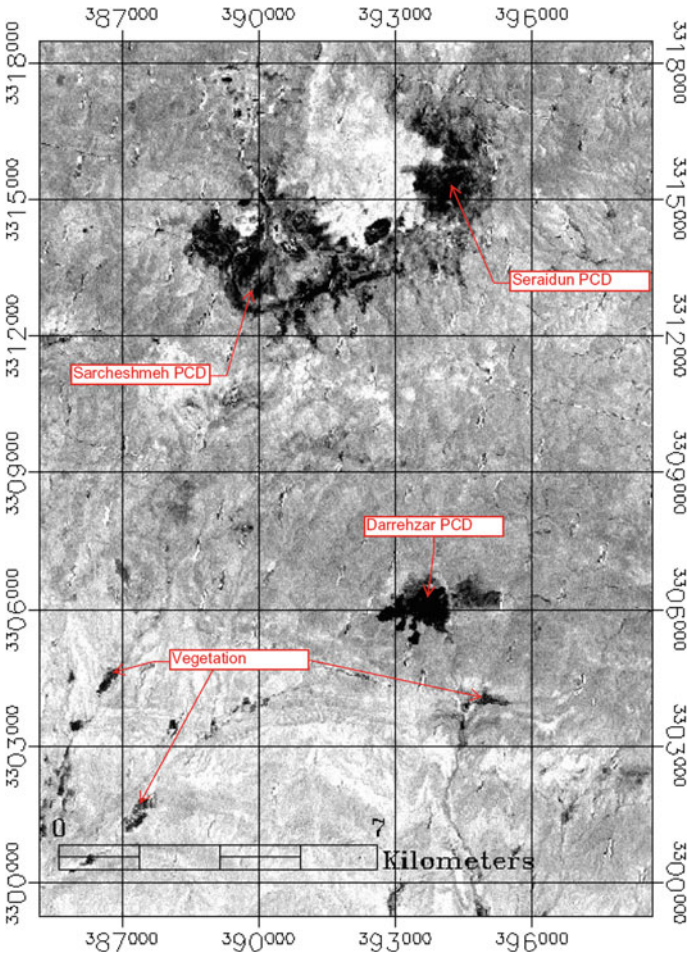

Fig. 4.16 PC4 image that shows altered areas with *black pixels*. The map coordinate is N, UTM, Zone 40, WGS84

produced extensive limonite and leaching of sulphide, giving a characteristic reddish or yellowish colour to the altered rocks. A weathered zone is developed a few metres to 80 metres below the surface (Fig. 4.15).

The eigenvector loadings and the eigenvalues are described in Table 4.5, using six ETM+ spectral bands. The first PC contains 88% of the variance of the six bands and gives information mainly on albedo and topography as all the bands have positive loadings. PC3 enhances vegetation cover in dark pixels, as the loading for band 9 is high and negative. PC4 enhances the hydroxyl minerals as both bands 5 and 7 have high loadings with opposite signs. Negative value for band 5 loading causes the altered parts to appear as dark pixels in Fig. 4.16. The vegetation cover also appears as dark pixels because of their water content that cause absorption in

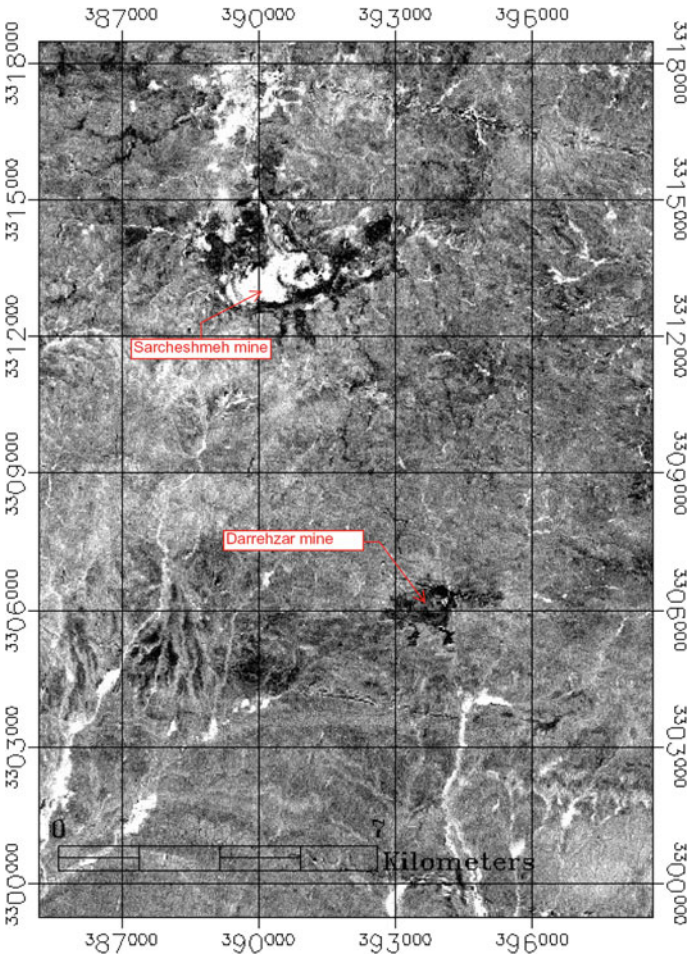

Fig. 4.17 PC4 image that shows iron oxide bearing areas with *black pixels*. The map coordinate is N, UTM, Zone 40, WGS84

band 7 of ETM+. PC5 enhances iron oxide minerals. Iron oxide minerals have higher reflectance in band 3 and absorption in band 1 of ETM+. Here both the bands have high loadings but with opposite signs. As the reflectance band has negative signs, the areas with iron oxide minerals appear in dark pixels (Fig. 4.17). Gossan or iron oxide cap rock is developed over the mineral deposits that have undergone the process of oxidation. Elements such as copper, molybdenum, Pb, Zn, etc. are leached out and iron oxide minerals such as hematite, goethite and jarosite are formed at the surface. This can be an indication of buried deposit. If you compare Figs. 4.16 and 4.17, it is noticed that the areas with hydrothermal

alteration also contain iron oxide minerals. The Sar Cheshmeh mine pit has alteration, but iron oxide minerals are extracted out and the mining activity is now in the supergene and hypogene parts. That is the reason that iron oxide is not seen over the mine pit.

4.4.2.3 Spectral Angle Mapper

Since our focus is on mineral exploration to map hydrothermal alteration haloes around porphyry copper mineralization, the spectra of selected alteration minerals from USGS spectral library were used as the end members and SWIR bands of ASTER data were used in the analysis. Muscovite (sericite) and illite is representative of phyllitic zone; kaolinite and montmorillonite are representative of argillic zone; and chlorite and epidote are representative of propylitic zone. Let's apply SAM method on Darrehzar area. The ASTER SWIR bands should be preprocessed before applying SAM. Internal average relative reflectance was applied on SWIR images. The preprocessed SWIR bands classified using SAM method (Fig. 4.18).

SAM classification method gave a good result that was very close to the reality for identification of alteration types in the area. When, we compare Figs. 4.13 and 4.18, it is clear that SAM classification has provided far better result than ratio image.

Govil (2015), used SAM method to map hydrothermally altered minerals around Askot basement mineralization of Kumoan Himalaya, India, using EO-1 hyperspectral data. Askot basemetal mineralization occurred in the Askot crystallines of the Kumaon Himalaya, India. In the Kumaon Himalaya at Askot copper deposit, the country rocks are crystallines which are underlain by younger formation of Inner Sedimentary Belt (ISB) of the region. Structurally, this is confined by Main Central Thrust in the north, and Almora Thrust in the South. As mentioned the crystallines rock comprise varieties of gneisses such as augen gneiss, granite gneiss,

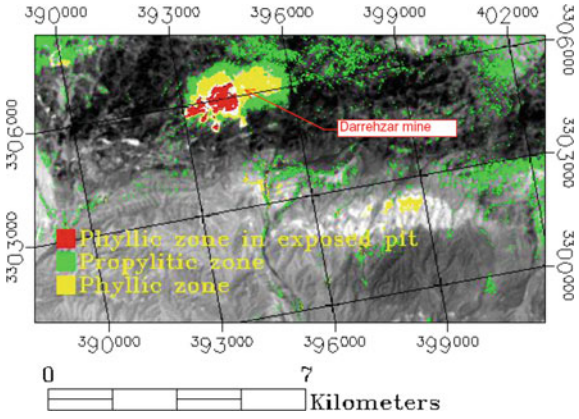

Fig. 4.18 Classified ASTER SWIR images using SAM. The map coordinate is N, UTM, Zone 40, WGS84

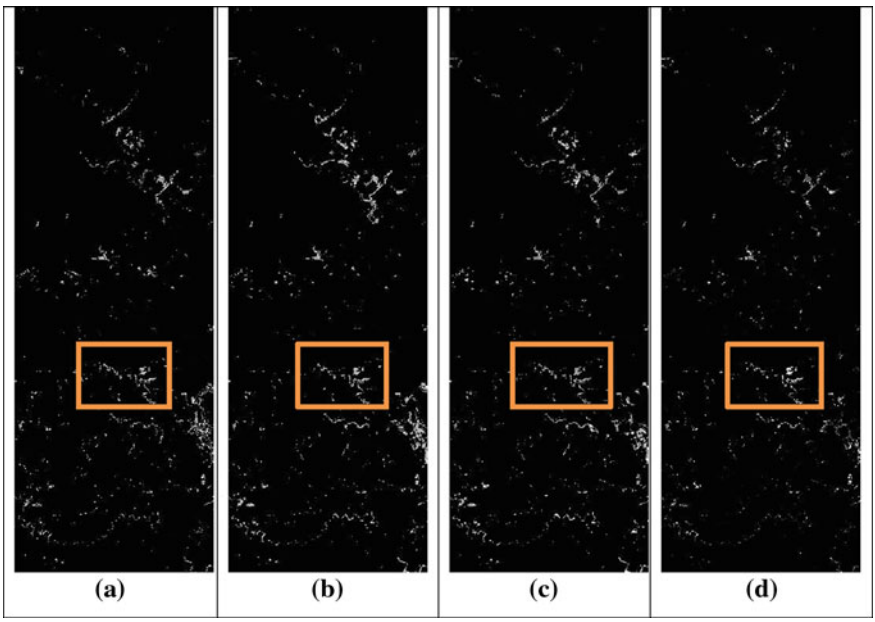

Fig. 4.19 Mineral map of the Askot basement mineralization. **a** Chlorite, **b** Goethite, **c** Illite, **d** Muscovite (Govil 2015)

garnetiferous-biotite gneiss, biotite-muscovite gneiss. In addition, calcsilicates and quartzites are also seen. Dykes of aplites and pegmatites are frequent (Govil 2015).

The Hyperion data was preprocessed and later on analyzed using SAM method (Govil 2015). Figure 4.19 shows the resulted images that depict the distribution of alteration minerals in the area.

These alteration maps providing the initial exploratory data that acts as basis for other exploratory techniques such as geophysics, geochemistry and drilling. They can provide necessary data to the exploration geologist for laying out the geophysical survey lines or choosing the area for geochemical sampling.

4.4.3 Application of Remote Sensing in Bauxite and Carbonate Exploration

Sanjeevi (2008) studied the potential of spectral analysis of multispectral satellite image data for targeting of mineral content in bauxite and limestone rich areas in southern India around Ariyalur and Kolli Hills areas. ASTER images have been used for this study. Image processing of ASTER data delineated areas rich in carbonates and alumina. Several geological and geomorphological parameters that control limestone and bauxite formation were also mapped using ASTER images.

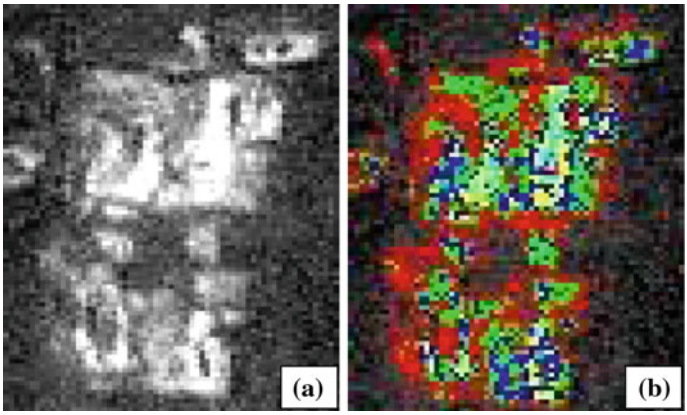

Fig. 4.20 **a** Carbonate fraction image and **b** density sliced fraction image; *red* <50%; *green* 50–60%; *blue* 60–70%; *yellow* 70–80%; *cyan* 80–90%; *white* >90% (Sanjeevi 2008) (color figure online)

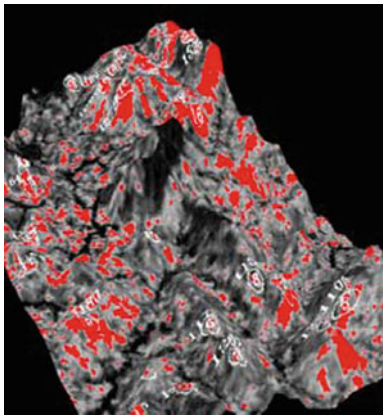

Fig. 4.21 Density sliced alumina fraction image draped over digital elevation model, showing location with 70–100% alumina (shown in *red*) (Sanjeevi 2008)

Figure 4.20 shows an image that shows $CaCO_3$ abundances which is derived from ASTER data. Figure 4.21 shows abundance map of bauxite that is derived from ASTER data.

4.4.4 Application of Remote Sensing in Exploration of Placer Deposits

In the southern state of Tamil Nadu in the peninsular India along the coast line occurs excellent deposit of heavy mineral beach placers. These deposits have been investigated by remote sensing (Fig. 4.22). Beside mineral exploration, remote

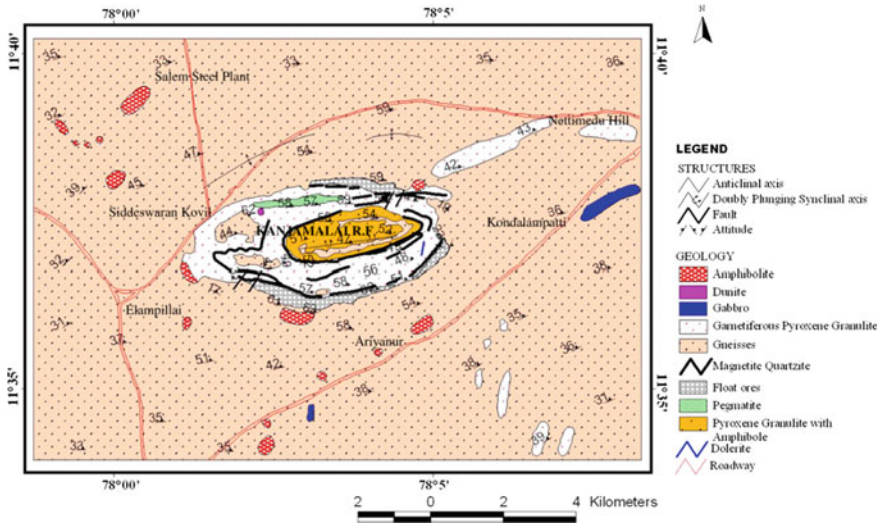

Fig. 4.22 Lithological map of Salem region (Rajendran et al. 2011)

sensing has also helped to identify environmental parameters for sustainable mining of these deposits. It has also guided to control coastal erosion.

4.4.5 Application of Remote Sensing for Iron Ore Exploration

In the high-grade granulite country around Salem, Rajendran et al. (2011) described a technique for discriminating iron ores (magnetite quartzite deposits) and associated lithology in high-grade granulite region of Salem, Southern Peninsular India using visible, near-infrared and short-wave infrared reflectance data of Remote Sensing—ASTER Image spectra has shown lithology very clearly. They comprise magnetite quartzite of garnetiferous pyroxene granulite, hornblende biotite gneiss, amphibolite, dunite and pegmatite have absorption features around spectral bands 1, 3, 5 and 7.

Deposits of iron ores here are banded iron formations rich in iron and iron silicates of meta-sedimentary rocks. A full geological succession is visible in Kanjamalai region of Salem (Fig. 4.23).

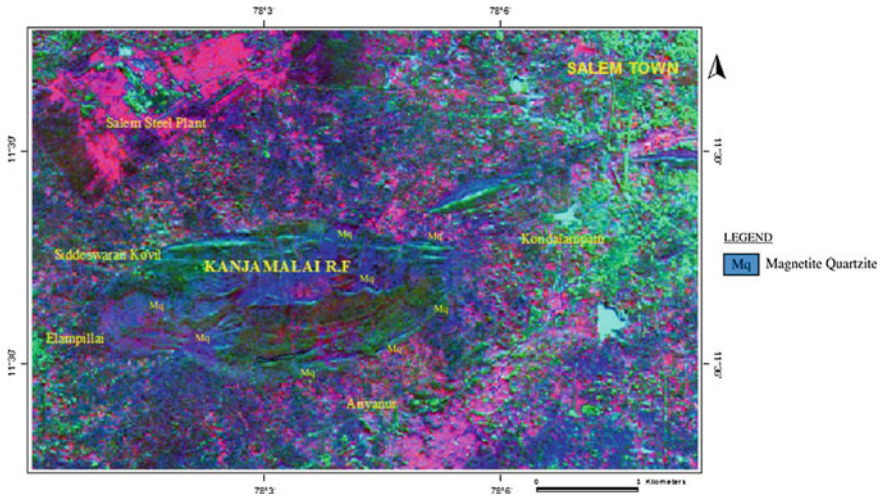

Fig. 4.23 Colour combination of band ratios ((1 + 3)/2, (3 + 5)/4, (5 + 7)/6) in *red*, *green* and *blue* (color figure online)

In case of iron oxide mineral exploration, the algorithm is relatively simple. Iron oxide minerals such as hematite, goethite and jarosite show an absorption trough in blue band and two reflection peaks at red and near-infrared parts of spectrum. Band 3/band1 ratio for landsat, band 2/band 1 ratio for IRS, SPOT and ASTER, can be used for enhancing these minerals. Other image processing methods such as PCA and SAM can also be used.

4.4.6 Remote Sensing Application for Chromite Exploration

Rajendran et al. (2012) have used ETM+ and ASTER data for chromite bearing mineralized zones in Semail ophiolite massifs of the northern Oman mountains. They used the capabilities of Landsat TM and Advanced Spaceborne Thermal Emission and Reflection Radiometer (ASTER) satellite data; applying image processing methods including non-correlated stretching, different band rationing and PCA for mapping chromite bearing areas. The study results show that the processed VNIR and SWIR spectral wavelength regions are promising in detecting the areas of potential chromite bearing mineralized zones within the ophiolite region, and proved to be successful for mapping of serpentinized harzburgite containing chromites. Figure 4.24 shows the colour combination of PC images that depicts several lithological units in the area.

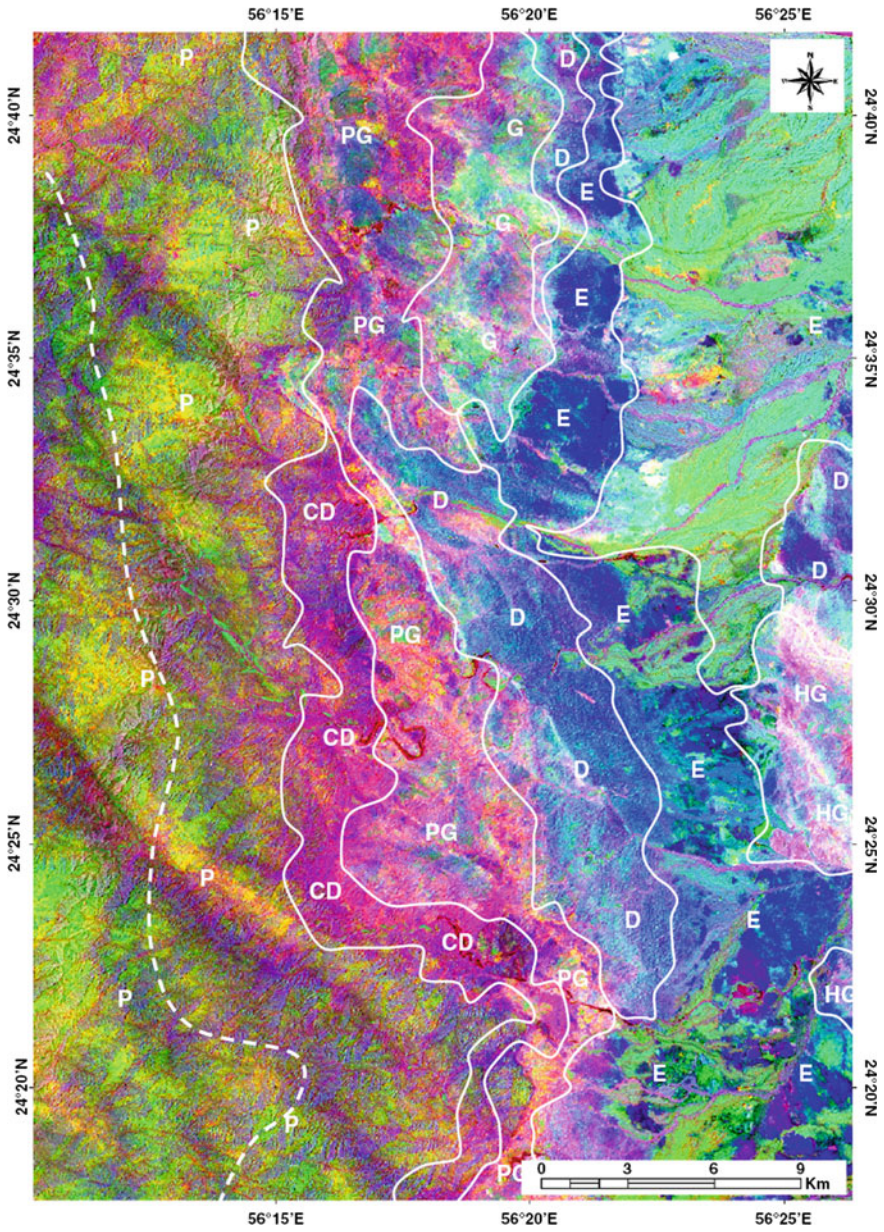

Fig. 4.24 Remote sensing image showing geology of the area; PC7, PC5 and PC4 of PCA bands. The index shows: *E* Basic extrusive rocks primarily spilites pillow lava, conglomerate; *D* Diabase dyke swarms; *G* Gabbro; *HG* Gabbroid hypabyssal rocks; *PG* Cumulate layered gabbro; *P* and *CD* Sheared serpentinized harzburgite (adopted from Rajendran et al. 2012)

Further Readings

Abrams MJ, Brown D, Lepley L, Sadowski R (1983) Remote sensing for porphyry copper deposits in southern Arizona. Econ Geol 78(4):591–604

Abrams M, Hook S, Ramachandran B (2002) ASTER user handbook (Ver. 2). Jet Propulsion Laboratory, California Institute of Technology, NASA, USA, p 135

Bernstein R (1983) Image geometry and rectification. In: Colwell RN (ed) Manual of remote sensing, 2nd edn. American Society of Photogrammetry, Falls Church, Virginia, pp 873–922

Chaves PS Jr, Berlin GL, Sowers LB (1982) Statistical method for selecting landsat MSS ratios. J Appl Photographic Eng 8:23–30

Campbell JB (2007) Introduction to remote sensing. The Guilford Press, New York, p 626

Carter WD, Rowen LC, Huntington JF (2013) Remote sensing in mineral exploration, Elsevier, Amsterdam, p. 186

Crosta AP, De Souza Filho CR, Azevedo F, Brodie C (2003) Targeting key alteration minerals in epithermal deposits in Patagonia, Argentina, using ASTER imagery and principal component analysis. Int J Remote Sens 24(21):4233–4240

Crosta A, Moore J (1990) Enhancement of Landsat Thematic Mapper imagery for residual soil mapping in SW Minas Gerais State, Brazil-A prospecting case history in greenstone belt terrain. In: Thematic conference on remote sensing for exploration geology—methods, integration, solutions, Calgary, Canada, pp 1173–1187

Di Tommaso I, Rubinstein N (2007) Hydrothermal alteration mapping using ASTER data in the Infiernillo porphyry deposit, Argentina. Ore Geol Rev 32(1):275–290

Dimitrijevic MD, Dimitrijevic MN, Djordjevic M, Vulovic D (1971) Geological map of the Pariz area, scale 1: 100,000. Geological Survey of Iran, Tehran

Drury SA, Hunt GA (1989) Geological uses of remotely-sensed reflected and emitted data of lateritized Archaean terrain in Western Australia. Int J Remote Sens 10(3):475–497

Drury SA (1993) Image interpretation in geology, 2nd edn. Allen and Unwin, London

Economic Geology (1983) An issue devoted to techniques and results of remote sensing. 78:573–770

Eklundh L, Singh A (1993) A comparative analysis of standardised and unstandardised principal components analysis in remote sensing. Int J Remote Sens 14(7):1359–1370

Fisher WA (1975) History of remote sensing. In: Reeves RG (ed) Manual of remote sensing. American Society Of Photogrametry, Falls Church, Virginia, pp 27–50

Galvao LS, Formaggio AR, Tisot DA (2005) Discrimination of sugarcane varieties in Southeastern Brazil with EO-1 Hyperion data. Remote Sens Environ 94(4):523–534

Govil H (2015) Identification and mapping of hydrothermally altered minerals in and around Askot base-metal mineralization of Kumoan Himalaya, India using EO-1 Hyperion data. Int J Adv Remote Sens GIS Geogr 3(1):1–8

Gupta RP (2008) Remote sensing geology. Springer, Berlin, p 655

Gupta RP (2013) Remote sensing geology. Springer Science & Business Media, Berlin

Honarmand M, Ranjbar H, Shahabpour J (2011) Application of spectral analysis in mapping hydrothermal alteration of the Northwestern Part of the Kerman Cenozoic Magmatic Arc, Iran, Journal of Sciences, Islamic Republic of Iran, 22(3): 221-238

Hubbard BE, Crowley JK (2005) Mineral mapping on the Chilean-Bolivian Altiplano using co-orbital ALI, ASTER and Hyperion imagery: data dimensionality issues and solutions. Remote Sens Environ 99(1):173–186

Hunt GR (1977) Spectral signatures of particulate minerals in the visible and near-infrared. Geophysics 42:501–513

Hunt GR, Ashley RP (1979) Spectra of altered rocks in the visible and near infrared. Econ Geol 74:1612–1629

Hunt GR, Salisbury JW (1970) Visible and near-infrared spectra of minerals and rocks: I silicate minerals. Modern Geol 1:283–300

Jensen JR (1996) Introductory digital image processing: a remote sensing approach. Prentice Hall, Upper Saddle River, NJ, p 7458

Kruse FA, Lefkoff AB, Boardman JW, Heidebrecht KB, Shapiro AT, Barloon PJ, Goetz AFH (1993) The spectral image processing system (SIPS)—interactive visualization and analysis of imaging spectrometer data. Remote Sens Environ 44(2):145–163

Kruse FA, Boardman JW, Huntington JF (2003) Comparison of airborne hyperspectral data and EO-1 Hyperion for mineral mapping. IEEE Trans Geosci Remote Sens 41(6):1388–1400

Lillesand TM, Kiefer RW (2003) Remote sensing and image interpretation. Wiley, New Jersey, p 722

Lillesand T, Kiefer RW, Chipman J (2014) Remote sensing and image interpretation. Wiley, New Jersey

Loughlin WP (1991) Principal component analysis for alteration mapping. Photogram Eng Remote Sens 57(9):1163–1169

Lowman PD (1969) Geologic orbital photography, experience from the Gemini program. Photogrametrica 24:77–106

Mars JC, Rowan LC (2006) Regional mapping of phyllic-and argillic-altered rocks in the Zagros magmatic arc, Iran, using Advanced Spaceborne Thermal Emission and Reflection Radiometer (ASTER) data and logical operator algorithms. Geosphere 2(3):161–186

Mather PM (1987) Computer processing of remotely-sensed images, an introduction. Wiley, New York, p 352

Navai I, Mehdizadeh-Tehrani S (1994) Alteration mapping by remote sensing techniques in south Iran, a case study. In: Proceedings of the 15th Asian conference on remote sensing, Bangalore, India

Navalgund RR, Jayaraman V, Roy PS (2007) Remote sensing applications: an overview. Curr Sci 93(12):1747–1766

Niblack W (1986) An introduction to digital image processing. Strandberg Publishing Company

Rajendran S, Thirunavukkarasu A, Balamurugan G, Shankar K (2011) Discrimination of iron ore deposits of granulite terrain of Southern Peninsular India using ASTER data. J Asian Earth Sci 41(1):99–106

Rajendran S, Al-Khirbash S, Pracejus B, Nasir S, Al-Abri AH, Kusky TM, Ghulam A (2012) ASTER detection of chromite bearing mineralized zones in Semail Ophiolite Massifs of the northern Oman Mountains: exploration strategy. Ore Geol Rev 44:121–135

Ranjbar H (2011) Remote sensing, applications to geophysics. In: Encyclopedia of solid earth geophysics. Springer, Netherlands, pp 1035–1039

Ranjbar H, Honarmand M (2007) Exploration for base metal mineralization in the southern part of the Central Iranian Volcanic Belt by using ASTER and ETM+ data. J Eng Sci 3:23–34

Ranjbar H, Roonwal GS (2002) Digital image processing for lithological and alteration mapping, using spot multispectral data. A case study of Pariz area, Kerman Province. In: Proceedings of SPIE, remote sensing for environmental monitoring, GIS applications, and geology, Iran, vol 4545

Rowan LC, Mars JC (2003) Lithologic mapping in the Mountain Pass, California area using advanced spaceborne thermal emission and reflection radiometer (ASTER) data. Remote Sens Environ 84(3):350–366

Rowan LC, Schmidt RG, Mars JC (2006) Distribution of hydrothermally altered rocks in the Reko Diq, Pakistan mineralized area based on spectral analysis of ASTER data. Remote Sens Environ 104(1):74–87

Sabins FF (1999) Remote sensing for mineral exploration. Ore Geol Rev 14(3):157–183

Sanjeevi S (2008) Targeting limestone and bauxite deposits in southern India by spectral unmixing of hyperspectral image data. Int Arch Photogram Remote Sens Spat Inf Sci 37:1189–1194

Shahriari H, Ranjbar H, Honarmand M (2013) Image segmentation for hydrothermal alteration mapping using PCA and concentration–area fractal model. Nat Resour Res 22(3):191–206

Tangestani MH, Moore F (2001) Porphyry copper potential mapping using the weights-of-evidence model in a GIS, northern Shahr-e-Babak, Iran. Aust J Earth Sci 48 (5):695–701

Tangestani MH, Moore F (2002) Porphyry copper alteration mapping at the Meiduk area. Iran. International Journal of Remote Sensing 23(22):4815–4825

Tangestani MH, Mazhari N, Agar B, Moore F (2008) Evaluating Advanced Spaceborne Thermal Emission and Reflection Radiometer (ASTER) data for alteration zone enhancement in a semi-arid area, northern Shahr-e-Babak, SE Iran. Int J Remote Sens 29(10):2833–2850

Van der Meer FD, Van der Werff HM, van Ruitenbeek FJ, Hecker CA, Bakker WH, Noomen MF, Woldai T (2012) Multi-and hyperspectral geologic remote sensing: A review. Int J Appl Earth Obs Geoinf 14(1):112–128

Zhang X, Pazner M, Duke N (2007) Lithologic and mineral information extraction for gold exploration using ASTER data in the south Chocolate Mountains (California). ISPRS J Photogram Remote Sens 62(4):271–282